

Response to the editor:

**Please clarify whether the response to referees 2's last comment about resolution applies for for priors of much higher resolution, say 2.5km.**

We clarify that finer resolution priors are desirable for retrieval accuracy and that our test is only applicable for inversions at the simulation resolution.

Line 323: “The  $SF_{finer}$  test indicates that although using a finer resolution model to generate *a priori* profiles is desirable for a more accurate retrieval, consistency between the simulation profile and the *a priori* shape factor is of greater importance explicitly for the purpose of simulation-observation comparisons to constrain emissions at the simulation resolution.”

1 **Effects of *a priori* profile shape assumptions on comparisons between satellite NO<sub>2</sub> columns**  
2 **and model simulations**

3

4 Matthew J. Cooper<sup>1,2</sup>, Randall V. Martin<sup>2,1,3</sup>, Daven K. Henze<sup>4</sup>, Dylan B.A. Jones<sup>5</sup>

5 1. Department of Physics and Atmospheric Science, Dalhousie University, Halifax, Nova Scotia,  
6 Canada

7 2. Department of Energy, Environmental & Chemical Engineering, Washington University in St.  
8 Louis, St. Louis, Missouri, USA

9 3. Harvard-Smithsonian Center for Astrophysics, Cambridge, Massachusetts, USA

10 4. Department of Mechanical Engineering, University of Colorado, Boulder, Colorado, USA

11 5. Department of Physics, University of Toronto, Toronto, Ontario, Canada

12

13 **Abstract**

14 A critical step in satellite retrievals of trace gas columns is the calculation of the air mass factor  
15 (AMF) used to convert observed slant columns to vertical columns. This calculation requires *a*  
16 *priori* information on the shape of the vertical profile. As a result, comparisons between satellite-  
17 retrieved and model-simulated column abundances are influenced by the *a priori* profile shape.  
18 We examine how differences between the shape of the simulated and *a priori* profile can impact  
19 the interpretation of satellite retrievals by performing an adjoint-based 4D-Var assimilation of  
20 synthetic NO<sub>2</sub> observations for constraining NO<sub>x</sub> emissions. We use the GEOS-Chem Adjoint  
21 model to perform assimilations using a variety of AMFs to examine how *a posteriori* emission  
22 estimates are affected if the AMF is calculated using an *a priori* shape factor that is inconsistent  
23 with the simulated profile. In these tests, an inconsistent *a priori* shape factor increased root  
24 mean square errors in *a posteriori* emission estimates by up to 30% for realistic conditions over  
25 polluted regions. As the difference between the simulated profile shape and the *a priori* profile  
26 shape increases, so do the corresponding assimilated emission errors. This reveals the importance  
27 of using simulated profile information for AMF calculations when comparing that simulated  
28 output to satellite retrieved columns.

29

30 **1. Introduction**

31 Satellite observations provide a wealth of information on the abundance of trace gases in  
32 the troposphere (Fishman et al., 2008). The next generation of satellite instruments, including the

33 upcoming geostationary constellation of TEMPO (Chance et al., 2013; Zoogman et al., 2017),  
34 Sentinel-4 (Bazalgette Courrèges-Lacoste et al., 2011; Ingmann et al., 2012), and GEMS (Bak et  
35 al., 2013; Kim, 2012), will provide information on NO<sub>2</sub> and other air quality relevant pollutants  
36 on unprecedented spatial and temporal scales. Insight into processes that affect atmospheric  
37 composition, including emissions (Streets et al., 2013), lifetimes (Fioletov et al., 2015; de Foy et  
38 al., 2015; Laughner and Cohen, 2019), and deposition (Geddes and Martin, 2017; Kharol et al.,  
39 2018) can be gained by interpreting this information with atmospheric chemistry models.

40         There are three main stages in retrieving trace gas abundances from ultraviolet and  
41 visible solar backscatter radiance measurements: calculating a light-path “slant column” by  
42 fitting observed spectra to known spectral signatures of trace gases, removing the stratospheric  
43 portion of the column, and converting the slant column to a vertical column density using an air  
44 mass factor (AMF). AMFs are calculated using a radiative transfer model and are a function of  
45 viewing geometry, surface reflectance, clouds, and radiative transfer properties of the  
46 atmosphere. AMF calculations also require an *a priori* estimate of the trace gas vertical profile  
47 and are sensitive to the profile shape (Eskes and Boersma, 2003; Palmer et al., 2001).  
48 Uncertainties in AMF calculations are the dominant source of uncertainty in satellite NO<sub>2</sub>  
49 retrievals over polluted regions (Boersma et al., 2007; Martin et al., 2002) largely due to  
50 sensitivity to surface reflectance, clouds, aerosols, and *a priori* profile information (Lorente et  
51 al., 2017).

52         Boersma et al. (2016) highlighted the issue of representativeness errors in comparing  
53 model simulated values with UV-Vis satellite-retrieved columns. Vertical representativeness  
54 errors arise from the satellite’s altitude-dependent sensitivity due to atmospheric scattering and  
55 can degrade the quality of model-measurement comparisons beyond errors that arise from either  
56 modeling or measurements alone. A consistent accounting of the altitude-dependent sensitivity is  
57 necessary to limit these errors.

58         Two common methods are used to account for vertical representativeness. In one method,  
59 observed slant columns are converted to vertical columns using an air mass factor calculated  
60 with scattering weights to represent instrument vertical sensitivity and shape factors to represent  
61 the vertical profile (Palmer et al., 2001). Another commonly used method employs an AMF  
62 provided with the retrieval to convert slant columns to vertical columns, and then applies an  
63 averaging kernel to the simulated profile to resample the simulated profile in a manner that

64 mimics the satellite vertical sensitivity (Eskes and Boersma, 2003). In this method both the  
65 averaging kernel and the retrieval AMF are calculated using an *a priori* NO<sub>2</sub> profile that may  
66 have a different shape than the simulated profile, which may introduce errors in the observation-  
67 simulation comparison (Zhu et al., 2016).

68 A common application of comparisons between satellite observed columns and model  
69 simulations is to constrain NO<sub>x</sub> emissions (e.g. Ding et al., 2018; Ghude et al., 2013; Lamsal et  
70 al., 2011; Martin et al., 2003; Vinken et al., 2014). One such approach is the use of four-  
71 dimensional variational (4D-Var) data assimilation, which seeks to minimize a cost function that  
72 accounts for the difference between simulated and retrieved values. As the cost function is a  
73 difference between observed and simulated NO<sub>2</sub> columns, it is susceptible to vertical  
74 representativeness errors resulting from inconsistent *a priori* vertical profile information.

75 In this work we examine how *a priori* profile assumptions impact satellite-model  
76 comparisons and use the GEOS-Chem adjoint as a case study to assess how this impact can  
77 affect the interpretation of satellite observations. Section 2 provides the mathematical framework  
78 for AMF calculations and satellite-model comparisons. Section 3 describes the adjoint model and  
79 synthetic observations for the case study. Section 4 discusses the results.

80

## 81 **2. Mathematical frameworks**

### 82 **2.1 AMFs and averaging kernels**

83 The air mass factor translates the line-of-sight slant column abundances ( $\Omega_s$ ) retrieved  
84 from satellite observed radiances into vertical column abundances ( $\Omega_v$ ). An air mass factor is the  
85 ratio of  $\Omega_s$  to  $\Omega_v$  and depends on the atmospheric path as determined by geometry, NO<sub>2</sub> vertical  
86 profile ( $\mathbf{n}$ ), surface reflectance, and radiative transfer properties of the atmosphere. Here we use  
87  $M(\mathbf{n})$  to represent an air mass factor derived using the vertical number density profile  $\mathbf{n}$ :

$$M(\mathbf{n}) = \frac{\Omega_s}{\Omega_v} \quad (1)$$

88

89 In the method described by Palmer et al. (2001), a radiative transfer model is used calculate  
90 scattering weights  $w(z)$  (also known as box air mass factors) which characterize the sensitivity of  
91 backscattered radiance  $I_B$  to the abundance of a trace gas at altitude  $z$ :

92

$$w(z) = -\frac{1}{M_G} \frac{\alpha_{a,z}}{\alpha_{eff}} \frac{\partial \ln(I_B)}{\partial \tau} \quad (2)$$

93 where  $\alpha_{a,z}$  is the temperature-dependent absorption cross section ( $\text{m}^2 \text{molec}^{-1}$ ),  $\alpha_{eff}$  is the effective  
 94 (weighted average) absorption cross section ( $\text{m}^2 \text{molec}^{-1}$ ) and  $\partial \tau$  is the incremental trace gas  
 95 optical depth.  $M_G$  represents a geometric path correction accounting for the satellite viewing  
 96 geometry:

$$M_G = \sec \theta_o + \sec \theta \quad (3)$$

97 where  $\theta$  is the solar zenith angle and  $\theta_o$  is the satellite viewing angle. This information is then  
 98 combined with an *a priori*  $\text{NO}_2$  shape factor (i.e. normalized vertical profile)

$$S(z) = \frac{\mathbf{n}(z)}{\Omega_v} \quad (4)$$

99 typically calculated with an atmospheric chemistry model to provide an air mass factor via:

100

$$M(\mathbf{n}) = \int_0^{\text{tropopause}} \mathbf{w}(z) S(z) dz \quad (5)$$

101 where  $S(z)$  is calculated using vertical profile  $\mathbf{n}(z)$ . An attribute of the formulation of Palmer et  
 102 al. (2001) is the independence of atmospheric radiative transfer properties  $\mathbf{w}(z)$  and the vertical  
 103 trace gas profile  $S(z)$ . The AMF definition in Equation (1) combined with Eq. (4) indicates that a  
 104 slant column can be calculated from a known vertical profile via:

$$\Omega_s = \int_0^{\text{tropopause}} \mathbf{w}(z) \mathbf{n}(z) dz \quad (6)$$

105

106 In an alternative formulation, the air mass factor is represented as part of an averaging  
 107 kernel. As formulated by Rodgers and Connor (2003), the averaging kernel ( $\mathbf{A}$ ) provides the  
 108 information needed to relate the retrieved quantity  $\hat{\mathbf{n}}$  to the true atmospheric profile  $\mathbf{n}$ :

109

$$\hat{\mathbf{n}} - \mathbf{n}_a = \mathbf{A}(\mathbf{n} - \mathbf{n}_a) \quad (7)$$

110 where  $\mathbf{n}_a$  is an assumed *a priori* profile of number density. The elements of the column  
 111 averaging kernel are related to the scattering weights by:

$$\mathbf{A}(z) = \frac{\mathbf{w}(z)}{M(\mathbf{n}_a)} \quad (8)$$

112 where  $M(\mathbf{n}_a)$  is an air mass factor calculated using *a priori* vertical profile information. It is

113 important to note that unlike scattering weights, averaging kernels depend on the *a priori*  
114 assumed vertical profile shape.

115 A lexicon is given in Table 1 as notation used to describe these treatments has varied  
116 across the literature. We choose  $M$  for air mass factor as a single letter is clearer in equations,  $w$   
117 for scattering weights to maintain the original formulation of Palmer et al. (2001),  $n$  for number  
118 density following IUPAC recommendations, and  $\Omega$  for column densities as is common in  
119 radiative transfer literature.

120 Figure 1 shows examples of typical shape factor, scattering weight, and averaging kernel  
121 profiles for a range of atmospheric conditions. NO<sub>2</sub> shape factors have significant variability;  
122 Shape factors peak near the surface in urban regions due to local pollution sources, but peak in  
123 the upper troposphere in more remote regions due to lightning. The shape of a scattering weight  
124 profile depends strongly on surface reflectance and cloud conditions. Sensitivity in the lower  
125 troposphere increases over reflective surfaces. Clouds increase sensitivity above due to their  
126 reflectance but shield the satellite from observing the atmosphere below. Averaging kernels have  
127 similarities with scattering weights but depend on both the shape of the prior and the satellite  
128 sensitivity. As AMF calculations are a convolution of the shape factor and the scattering weight  
129 profiles, these shapes affect NO<sub>2</sub> retrievals. For these examples, the AMF for a clear sky  
130 observation with surface reflectance of 0.01 can range from 0.7 in an urban region to 1.7 in a  
131 remote region. This large difference demonstrates the importance of the assumed profile shape to  
132 the retrieval process.

133

## 134 **2.2 Comparing satellite observations to simulated values**

135

136 The following section expresses mathematically how satellite-model comparisons are made  
137 using various *a priori* profiles.

138

### 139 **2.2.1 Using scattering weights**

140 Following Palmer et al. (2001), a retrieved vertical column ( $\widehat{\Omega}_{v,o}$ ) is estimated using an  
141 observed slant column  $\Omega_{s,o}$  and a simulation-based air mass factor  $M(\mathbf{n}_m)$ , which can be  
142 calculated with Eq. (5) using the model-simulated NO<sub>2</sub> profile ( $\mathbf{n}_m$ ):

143

$$\widehat{\Omega}_{v,o} = \frac{\Omega_{s,o}}{M(\mathbf{n}_m)} \quad (9)$$

144

145 The difference  $\Delta_m$  between the estimated retrieved column and the model-simulated vertical  
 146 column ( $\Omega_{v,m}$ ) is:

$$\Delta_m = \Omega_{v,m} - \widehat{\Omega}_{v,o} \quad (10)$$

$$\Delta_m = \left( \sum_0^{tropopause} n_m \right) - \frac{\Omega_{s,o}}{M(\mathbf{n}_m)} \quad (11)$$

147 Equation (11) describes how this comparison is used in practice. However, we can rearrange this  
 148 expression in terms of model ( $\Omega_{s,m}$ ) and observed ( $\Omega_{s,o}$ ) slant columns using the definition of air  
 149 mass factor:

$$\Delta_m = \frac{\Omega_{s,m}}{M(\mathbf{n}_m)} - \frac{\Omega_{s,o}}{M(\mathbf{n}_m)} \quad (12)$$

$$\Delta_m = \frac{1}{M(\mathbf{n}_m)} (\Omega_{s,m} - \Omega_{s,o}) \quad (13)$$

150

## 151 2.2.2 Using averaging kernels

152

153 Comparison of simulated and retrieved columns using the averaging kernel is described  
 154 by Eskes and Boersma (2003) and in the retrieval documentation in Boersma et al. (2011). The  
 155 averaging kernel is applied to the simulated profile in order to sample the simulated column in a  
 156 manner that reflects the retrieval sensitivity:

$$\widehat{\Omega}_{v,m} = \sum_0^{tropopause} \mathbf{A} \mathbf{n}_m \quad (14)$$

157 The resampled simulated column is then compared to the retrieved vertical column ( $\Omega_{v,o}$ ) using  
 158 the *a priori*-based air mass factor  $M(\mathbf{n}_a)$  supplied with the retrieval dataset:

159

$$\Delta_a = \widehat{\Omega}_{v,m} - \Omega_{v,o} \quad (15)$$

$$\Delta_a = \left( \sum_{i=0}^{tropopause} \mathbf{A}_i \mathbf{n}_{m,i} \right) - \frac{\Omega_{s,o}}{M(\mathbf{n}_a)} \quad (16)$$

160 Equation (16) describes how this method is used in practice. To facilitate the comparison with  
 161 Eq. (13), Eq. (16) can be rewritten using an alternative formulation relating averaging kernels to  
 162 scattering weights:

163

$$\Delta_a = \left( \sum_{i=0}^{tropopause} \frac{\mathbf{w}_i \mathbf{n}_{m,i}}{M(\mathbf{n}_a)} \right) - \frac{\Omega_{s,o}}{M(\mathbf{n}_a)} \quad (17)$$

$$\Delta_a = \frac{1}{M(\mathbf{n}_a)} (\Omega_{s,m} - \Omega_{s,o}) \quad (18)$$

164

165 By comparing Eq. (13) to Eq. (18), it is evident that the underlying difference between the two  
 166 approaches is the choice of *a priori* profile information used to calculate the AMF, as the  
 167 averaging kernel method is not independent of *a priori* profile assumptions. This bias could be  
 168 addressed by replacing the *a priori* -based AMF in Eq. (18) with a simulation-based AMF using  
 169 the following relationship (Boersma et al., 2016; Lamsal et al., 2010):

$$M(\mathbf{n}_m) = M(\mathbf{n}_a) \frac{\sum \mathbf{A} \mathbf{n}_m}{\sum \mathbf{n}_m} \quad (19)$$

170 It should be noted that both the averaging kernel and scattering weight methods are  
 171 equivalent for comparisons that examine ratios of retrieved and modeled columns:

$$r_m = \frac{\widehat{\Omega}_{v,o}}{\Omega_{v,m}} = \frac{\Omega_{s,o} / M(\mathbf{n}_m)}{\sum \mathbf{n}_m} = \frac{\Omega_{s,o}}{\sum \mathbf{n}_m} \frac{\sum \mathbf{n}_m}{\sum \mathbf{w} \mathbf{n}_m} = \frac{\Omega_{s,o}}{\sum \mathbf{w} \mathbf{n}_m} \quad (20)$$

$$r_a = \frac{\Omega_{v,o}}{\widehat{\Omega}_{v,m}} = \frac{\Omega_{s,o} / M(\mathbf{n}_a)}{\sum \mathbf{A} \mathbf{n}_m} = \frac{\Omega_{s,o} / M(\mathbf{n}_a)}{\sum \mathbf{w} \mathbf{n}_m / M(\mathbf{n}_a)} = \frac{\Omega_{s,o}}{\sum \mathbf{w} \mathbf{n}_m} \quad (21)$$

172

173 For ratios, both methods are dependent on geophysical assumptions used to calculate scattering  
 174 weights but are independent of *a priori* profile information. Lastly, some studies (e.g., Buscela et  
 175 al., 2013; Qu et al., 2017) may directly assimilate slant column densities rather than vertical  
 176 column densities using

$$\Delta_{s,a} = \widehat{\Omega}_{s,m} - \Omega_{s,o} \quad (22)$$

$$= \left( \sum_{i=0}^{tropopause} \mathbf{w}_i \mathbf{n}_{m,i} \right) - \Omega_{s,o} \quad (23)$$

177 This approach is also still dependent upon the scattering weights but not upon external *a priori*  
 178 profile information. Overall, the choice of approach may be influenced by whether or not



179 scattering weights are available from either the NO<sub>2</sub> retrieval product or radiative transfer  
180 calculations applied to the model. In contrast, use of Eq. (11) or (16) are applicable when these  
181 are not explicitly available or provided.

182

### 183 **3. Tools and Methodology**

#### 184 **3.1 GEOS-Chem and its adjoint**

185 The GEOS-Chem chemical transport model ([www.geos-chem.org](http://www.geos-chem.org)) is used to create  
186 synthetic NO<sub>2</sub> observations and for their analysis. The GEOS-Chem version used here is version  
187 35j of the GEOS-Chem Adjoint model. GEOS-Chem includes a detailed oxidant-aerosol  
188 chemical mechanism (Bey et al., 2001; Park et al., 2004) and uses assimilated meteorological  
189 fields from the Goddard Earth Observation System (GEOS-5), with 47 vertical levels up to 0.01  
190 hPa and a horizontal resolution of 4°x5°. Global anthropogenic NO<sub>x</sub> emissions are provided by  
191 the Emission Database for Global Atmospheric Research (EDGAR) inventory (Olivier et al.,  
192 2005) with regional overwrites over North America (EPA/NEI99), Europe (EMEP), Canada  
193 (CAC), Mexico (BRAVO, (Kuhns et al., 2005)), and East Asia (Streets et al., 2006). Other NO<sub>x</sub>  
194 sources include biomass burning (GFED2 (Van der Werf et al., 2010)), lightning (Murray et al.,  
195 2012), and soils (Wang et al., 1998). This model has been used previously to constrain NO<sub>x</sub>  
196 emissions (Cooper et al., 2017; Henze et al., 2009; Qu et al., 2017, 2019; Xu et al., 2013; Zhang  
197 et al., 2016).

198 The GEOS-Chem adjoint (Henze et al., 2007, 2009) is used here to perform a 4D-Var  
199 data assimilation. The adjoint seeks to iteratively minimize a cost function generally defined by  
200 the difference between satellite retrieved and simulated columns ( $\Delta$ , from either Eq. (11) if using  
201 a simulation-based air mass factor or Eq. (16) if using the retrieval *a priori*-based air mass  
202 factor):

$$J = \frac{1}{2} \Delta^T S_o^{-1} \Delta + \frac{1}{2} \gamma_R (E - E_a)^T S_E^{-1} (E - E_a) \quad (24)$$

203 where  $E$  and  $E_a$  are the *a posteriori* and *a priori* emissions,  $S_o$  and  $S_E$  are the retrieval and *a*  
204 *priori* emission error covariance matrices, and  $\gamma_R$  is a regularization parameter that allows for  
205 weighting the cost function towards the retrieved columns or *a priori* emissions. Tests performed  
206 here required 20-30 iterations to minimize the cost function.

207

## 208 3.2 Experiment Outline

209 In this study we perform 4D-Var data assimilation experiments to infer surface NO<sub>x</sub>  
210 emissions using synthetic NO<sub>2</sub> observations. We use synthetic observations built from known  
211 emission inventories to provide a “truth” that can be used to evaluate the inversion results. To  
212 demonstrate how *a priori* profile information can propagate in an assimilation, we use either the  
213 model profile ( $\Delta_m$ , Eq. (11)) or an *a priori* profile ( $\Delta_a$ , Eq. (16)) in the cost function. A one-week  
214 spin-up window at the start of each adjoint iteration is used to allow NO<sub>x</sub> to reach steady state.  
215 Observation error covariances  $S_o$  are described as a relative error of 30% of the slant column  
216 density, plus an absolute error of  $10^{15}$  molecules cm<sup>-2</sup>, which is representative of typical satellite  
217 retrieved NO<sub>2</sub> column uncertainties (Boersma et al., 2007; Martin et al., 2002). We omit the *a*  
218 *priori* emissions constraint in the cost function (i.e. set  $\gamma_R=0$ ) to isolate the impact of the  
219 observations.

220

### 221 3.2.1 Synthetic observations

222 Synthetic observations ( $Obs_S$ ) are created using a GEOS-Chem simulation where random  
223 Gaussian noise with a standard deviation of 5% is added to the anthropogenic NO<sub>x</sub> emissions.  
224 Additional tests using observations where noise with a standard deviation of 30% is added  
225 ( $Obs_{30}$ ) are also used. No additional noise is added to the individual observations to isolate the  
226 impact of AMF errors against additional sources of uncertainty. Figure 2 shows the standard (*a*  
227 *priori*) anthropogenic NO<sub>x</sub> emissions and the changes used to create the “true” emissions for the  
228 synthetic observations.

229 For these tests, we use one observation per hour per 4°x5° grid box for a period of two  
230 weeks in July 2010. Observations consist of synthetic slant columns ( $\Omega_{s,o}$ ) created by applying  
231 scattering weights to the synthetic vertical profiles using Eq. (6). Scattering weights are  
232 calculated using the LIDORT radiative transfer model (Spurr, 2002) by providing LIDORT with  
233 the observation conditions of OMI observations during July 2010, which are used to represent  
234 typical viewing conditions of low earth orbit satellite observations, and aerosol profiles from the  
235 GEOS-Chem base simulation. To represent typical conditions, these representative scattering  
236 weight profiles for each grid box are used to produce the synthetic slant columns. Tests  
237 performed for all 4°x5° grid boxes used here indicate that the mean relative difference between  
238 an air mass factor calculated using an average scattering weight profile and the average of air

239 mass factors using observation-specific scattering weight profiles is less than 4%.

240

### 241 **3.2.2 Shape Factors**

242 To test the impact of *a priori* profile information, seven different tests are performed  
243 using seven different NO<sub>2</sub> profile shapes for AMF calculations:

- 244 • Case  $SF_M$ : The GEOS-Chem model simulated profile ( $n_m$ ), updated at each iteration  
245 of the adjoint run
- 246 • Case  $SF_{prior}$ : The *a priori* GEOS-Chem simulated profile, without updating.
- 247 • Case  $SF_{n30}$ : An *a priori* profile created by a GEOS-Chem simulation where global  
248 anthropogenic NO<sub>x</sub> emissions were perturbed with random Gaussian noise with a  
249 standard deviation of 30%. In cases where this results in negative emissions, a value  
250 of zero is used.
- 251 • Case  $SF_{diffem}$ : An *a priori* profile created by a GEOS-Chem simulation where regional  
252 emission overwrites are turned off.
- 253 • Case  $SF_{finer}$ : An *a priori* profile created by a GEOS-Chem simulation run at finer  
254 ( $2^\circ \times 2.5^\circ$ ) resolution.
- 255 • Case  $SF_{trop}$ : An *a priori* profile that assumes the NO<sub>2</sub> profile shape is uniform from  
256 the surface to the tropopause (~200 hPa).
- 257 • Case  $SF_{BL}$ : An *a priori* profile that assumes the NO<sub>2</sub> profile shape is uniform from the  
258 surface to the boundary layer (~800 hPa).

259

260 An advantage of using scattering weights and the simulated shape factor in a 4D-Var framework  
261 is that it allows for the shape factor, and thus the AMF, to be updated at each iteration. When *a*  
262 *priori* profiles from an external source are used it is not possible for them to update during the  
263 inversion. The  $SF_M$  and  $SF_{prior}$  cases test the impact that iterative updates to the AMF have on *a*  
264 *posteriori* estimates. The additional cases test for the impact of using an averaging kernel based  
265 on *a priori* profile assumptions that are inconsistent with the model. In practice, averaging  
266 kernels and *a priori* profiles included in retrieval data sets are generally derived from chemical  
267 transport models that have different physical processes, emissions, or spatial resolutions. The  
268  $SF_{n30}$  and  $SF_{diffem}$  tests are representative of inversions that use *a priori* profile information from  
269 a different chemical transport model with similar resolution but different emissions. The  $SF_{finer}$

270 test represents an inversion that uses *a priori* profiles from a chemical transport model with a  
271 different horizontal resolution. The  $SF_{BL}$  and  $SF_{trop}$  tests do not represent any modern retrieval  
272 algorithms, but are used as extreme examples of an *a priori* that assumes no spatial variability.  
273 The  $SF_{BL}$  profile is representative of polluted regions as indicated by the typical urban profile in  
274 Fig. 1, while the  $SF_{trop}$  profile is representative of a typical rural profile. Table 2 provides global  
275 mean AMFs for these test cases, which range from 1.3-2.1, and the resulting global mean  
276 observed vertical columns, which range from  $0.9-1.5 \times 10^{15}$  molec/cm<sup>2</sup>. Global mean ‘observed’  
277 vertical columns are 33% higher for  $SF_{2x25}$  than for  $SF_M$ , and up to 66% higher for  $SF_{BL}$ . Global  
278 mean ‘observed’ vertical columns for  $SF_{n30}$  and  $SF_{diffem}$  are similar to  $SF_M$ , although individual  
279 observations may differ by up to 18% for  $SF_{n30}$  and 28% for  $SF_{diffem}$ .

280

#### 281 4. Results

282 Figure 3 shows root mean square errors (RMSE) for the *a posteriori* emissions estimated  
283 by the 4D-Var assimilations of  $Obs_5$  synthetic observations. All tests successfully reduce the *a*  
284 *priori* emission error by an order of magnitude or more. The  $SF_M$  has the lowest RMSE  
285 indicating that it can best estimate the “true” emissions. The next lowest RMSE is for the  $SF_{prior}$   
286 test, which uses the same initial model shape factor but does not update during the adjoint  
287 iterations, followed by the  $SF_{finer}$ ,  $SF_{diffem}$ ,  $SF_{n30}$ ,  $SF_{trop}$ , and  $SF_{BL}$  tests.

288 Figure 4 shows maps of the difference in RMSE between the  $SF_M$  test and the other tests  
289 for  $Obs_5$  observations. The  $SF_M$  test has a lower RMSE than the other tests in 65-72% grid boxes  
290 where the difference is nonzero. Again, the  $SF_{prior}$  test is closest to the  $SF_M$  test with a root mean  
291 square difference of  $2.9 \times 10^7$  molec/cm<sup>2</sup>/s, followed by  $SF_{finer}$  ( $3.6 \times 10^7$  molec/cm<sup>2</sup>/s),  $SF_{n30}$   
292 ( $3.8 \times 10^7$  molec/cm<sup>2</sup>/s),  $SF_{diffem}$  ( $4.0 \times 10^7$  molec/cm<sup>2</sup>/s),  $SF_{trop}$ , ( $7.8 \times 10^7$  molec/cm<sup>2</sup>/s), and  $SF_{BL}$   
293 ( $9.0 \times 10^7$  molec/cm<sup>2</sup>/s).

294 Table 3 summarizes additional error statistics focused on grid boxes with significant  
295 emission sources. Errors in *a posteriori* emission estimates are correlated with the “true”  
296 emissions in the  $SF_{trop}$  and  $SF_{n30}$  tests, and weakly correlated in the  $SF_{BL}$ ,  $SF_{prior}$ , and  $SF_{diffem}$   
297 tests, indicating that these tests are not well constraining the emissions. Differences between tests  
298 are more significant over polluted regions where AMF errors are more influential; For example,  
299 in the regions with the highest NO<sub>x</sub> emissions, RMSE values indicate  $SF_M$  outperforms  $SF_{n30}$  by  
300 30% and  $SF_{trop}$  by >80%. Another sign of adjoint inversion quality is a low variance in errors.

301 While the posterior error is reduced relative to the *a priori* error in all tests, error standard  
302 deviations are 30% higher for  $SF_{n30}$  and 90% higher for  $SF_{trop}$  compared to  $SF_M$ . The global  
303 maximum error for the  $SF_{trop}$  test is 30% higher than for the  $SF_M$  test. All metrics indicate that  
304 the  $SF_M$  test best represents the “true” emissions.

305 Tests using  $Obs_{30}$  observations and the  $SF_M$  and  $SF_{trop}$  shape factors were also performed.  
306 Despite the difference between *a priori* observed vertical columns using these shape factors as  
307 indicated by Table 2, these assimilations produced similar *a posteriori* results, with RMSE of  
308  $2.9 \times 10^8$  molec/cm<sup>2</sup>/s for  $SF_M$  and  $2.8 \times 10^8$  molec/cm<sup>2</sup>/s for  $SF_{trop}$ .

309

## 310 5. Discussion & Conclusions

311 Accounting for the vertical profile dependence of satellite observations is essential to  
312 accurately interpret those observations. This work examines how the choice of shape factor  
313 affects differences between simulated and satellite-retrieved quantities in a data assimilation  
314 framework. Examination of the mathematical frameworks behind two common methods for  
315 comparing simulated and retrieved columns highlights how the method introduced by Palmer et  
316 al. (2001) facilitates separation of observation sensitivity (scattering weights) from the profile  
317 shape (shape factor) enabling the model-retrieval comparison to be independent of *a priori*  
318 profile assumptions.

319 In these case studies, vertical representativeness errors were best reduced by using a  
320 shape factor that was consistent with the model simulation. This was especially true in polluted  
321 regions where the AMF errors dominate observation uncertainties, as deviations between the  
322 tests were largest in these regions. The further the shape factor deviated from the model state the  
323 larger the inversion errors became, as indicated by Fig. 5. The  $SF_{finer}$  test indicates that although  
324 using a ~~fin~~higher resolution model to generate *a priori* profiles is desirable for a more accurate  
325 retrieval, ~~does not provide an advantage in simulation-observation comparisons, as~~ consistency  
326 between the simulation profile and the *a priori* shape factor is of greater importance explicitly  
327 for the purpose of simulation-observation comparisons to constrain emissions at the simulation  
328 resolution. Comparing the  $SF_M$  and  $SF_{prior}$  tests shows that allowing for the shape factor to update  
329 during the iterative adjoint process further reduces the RMSE by 10%. However, even without  
330 allowing for shape factor updates, using a shape factor that is consistent with the initial model  
331 state produces a more accurate inversion result than using other assumed profile shapes.

332 The case study presented here demonstrates that the shape factor source can have a strong  
333 influence on adjoint inversion results. However, the magnitude of this influence can vary.  
334 Inversion tests performed using synthetic observations based on random 30% perturbations to  
335 emissions were insensitive to the AMF, despite large differences in *a priori* vertical column  
336 densities. In these tests, the cost function was more sensitive to the larger difference between the  
337 observed and simulated slant columns (i.e.  $\Omega_{s,m} - \Omega_{s,o}$  in Eq. (13) and (19)) than to the AMF. This  
338 indicates that while the cost function is mathematically dependent on the AMF, the inversion is  
339 less sensitive to vertical representativeness errors in cases where emissions are poorly  
340 constrained, as is the case in recent adjoint inversion studies (e.g. Qu et al., 2017). However,  
341 choice of AMF will become increasingly important to adjoint inversions as emission inventories  
342 improve. Furthermore, omitting the *a priori* emissions constraint in the cost function and  
343 omitting noise in the observations in these tests to isolate the impact of the AMF effectively  
344 assumes poorly constrained *a priori* emissions and ideal observations. In practice, cost function  
345 sensitivity to AMF choice may be buffered when *a priori* emissions uncertainties and  
346 observational noise are considered.

347 As it is beneficial for a consistent shape factor to be used when comparing satellite  
348 retrieved values to model simulated results, it will be useful for data products to provide the  
349 information required for this method to the user community. This is most straightforward when  
350 scattering weights (rather than averaging kernels) are provided alongside retrieved column data,  
351 as scattering weights and shape factors are independently calculated, however simulation-based  
352 air mass factors can be calculated using the averaging kernel and *a priori*-based air mass factor  
353 via Eq. 19.

354 In summary, when comparing a model simulation to a satellite retrieved NO<sub>2</sub> column in a  
355 data assimilation environment utilizing column differences, calculating the AMF using the  
356 simulated shape factor allows for better accuracy in inversion results. This demonstration can  
357 provide general guidance for other methods of interpreting satellite observations with models, as  
358 using the simulated shape factor assures consistency in the vertical representativeness between  
359 model and retrieval.

360

## 361 **6. Author Contributions**

362 MJC and RVM designed the overall study. MJC designed and carried out the case studies and

363 their analysis. All co-authors provided guidance in analyzing results. MJC prepared the  
364 manuscript with contributions from all co-authors.

365

## 366 **7. Competing interests**

367 The authors declare that they have no conflict of interest.

368

## 369 **8. Acknowledgements**

370 This work was supported by the Canadian Space Agency. DH acknowledges support from  
371 NASA NNX17AF63G.

372

## 373 **9. Data Availability**

374 The GEOS-Chem chemical transport model and its adjoint are available at [www.geos-chem.org](http://www.geos-chem.org)  
375 (last access: 20 August 2017). OMI NO<sub>2</sub> data used in this study is available from the NASA  
376 Goddard Earth Sciences Data and Information Services Center (<https://disc.sci.gsfc.nasa.gov>;  
377 last access: 14 March 2019). AMF code (Spurr, 2002; Martin et al., 2002) used to calculate  
378 scattering weights and air mass factors is available at <http://fizz.phys.dal.ca/~atmos> (last access:  
379 19 June 2017).

380

## 381 **11. References**

382 Bak, J., Kim, J. H., Liu, X., Chance, K. and Kim, J.: Geoscientific Instrumentation Methods and  
383 Data Systems Evaluation of ozone profile and tropospheric ozone retrievals from GEMS and  
384 OMI spectra, *Atmos. Meas. Tech.*, 6, 239–249, doi:10.5194/amt-6-239-2013, 2013.

385 Bazalgette Courrèges-Lacoste, G., Ahlers, B., Guldimann, B., Short, A., Veihelmann, B. and  
386 Stark, H.: The Sentinel-4/UVN instrument on-board MTG-S, in EUMETSAT Meteorological  
387 Satellite Conference, Oslo, Norway., 2011.

388 Bey, I., Jacob, D. J., Yantosca, R. M., Logan, J. A., Field, B. D., Fiore, A. M., Li, Q., Liu, H. Y.,  
389 Mickley, L. J. and Schultz, M. G.: Global modeling of tropospheric chemistry with assimilated  
390 meteorology: Model description and evaluation, *J. Geophys. Res. Atmos.*, 106(D19), 23073–  
391 23095, 2001.

392 Boersma, K., Braak, R. and van der A, R. J.: Dutch OMI NO<sub>2</sub> (DOMINO) data product v2. 0,  
393 Tropospheric Emissions Monitoring Internet Service on-line documentation, [online] Available  
394 from: [http://www.temis.nl/docs/OMI\\_NO2\\_HE5\\_2.0\\_2011.pdf](http://www.temis.nl/docs/OMI_NO2_HE5_2.0_2011.pdf), 2011.

395 Boersma, K. F., Eskes, H. J., Veefkind, J. P., Brinksma, E. J., van der A, R. J., Sneep, M., van

396 den Oord, G. H. J., Levelt, P. F., Stammes, P., Gleason, J. F. and Bucsela, E. J.: Near-real time  
397 retrieval of tropospheric NO<sub>2</sub> from OMI, *Atmos. Chem. Phys.*, 7(8), 2103–2118,  
398 doi:10.5194/acp-7-2103-2007, 2007.

399 Boersma, K. F., Vinken, G. C. M. and Eskes, H. J.: Representativeness errors in comparing  
400 chemistry transport and chemistry climate models with satellite UV–Vis tropospheric column  
401 retrievals, *Geosci. Model Dev*, 9, 875–898, doi:10.5194/gmd-9-875-2016, 2016.

402 Chance, K., Liu, X., Suleiman, R. M., Flittner, D. E., Al-Saadi, J. and Janz, S. J.: Tropospheric  
403 emissions: monitoring of pollution (TEMPO), edited by J. J. Butler, X. (Jack) Xiong, and X. Gu,  
404 p. 88660D, International Society for Optics and Photonics., 2013.

405 Cooper, M., Martin, R. V., Padmanabhan, A. and Henze, D. K.: Comparing mass balance and  
406 adjoint methods for inverse modeling of nitrogen dioxide columns for global nitrogen oxide  
407 emissions, *J. Geophys. Res. Atmos.*, doi:10.1002/2016JD025985, 2017.

408 Ding, J., van der A, R. J., Mijling, B., Jalkanen, J.-P., Johansson, L. and Levelt, P. F.: Maritime  
409 NO<sub>x</sub> Emissions Over Chinese Seas Derived From Satellite Observations, *Geophys. Res. Lett.*,  
410 45(4), 2031–2037, doi:10.1002/2017GL076788, 2018.

411 Eskes, H. J. and Boersma, K. F.: Averaging kernels for DOAS total-column satellite retrievals,  
412 *Atmos. Chem. Phys.*, 3(5), 1285–1291, 2003.

413 Fioletov, V. E., McLinden, C. A., Krotkov, N. and Li, C.: Lifetimes and emissions of SO<sub>2</sub> from  
414 point sources estimated from OMI, *Geophys. Res. Lett.*, 42(6), 1969–1976,  
415 doi:10.1002/2015GL063148, 2015.

416 Fishman, J., Al-Saadi, J. A., Creilson, J. K., Bowman, K. W., Burrows, J. P., Richter, A.,  
417 Chance, K. V., Edwards, D. P., Martin, R. V., Morris, G. A., Pierce, R. B., Ziemke, J. R.,  
418 Schaack, T. K., Thompson, A. M., Fishman, J., Al-Saadi, J. A., Creilson, J. K., Bowman, K. W.,  
419 Burrows, J. P., Richter, A., Chance, K. V., Edwards, D. P., Martin, R. V., Morris, G. A., Pierce,  
420 R. B., Ziemke, J. R., Schaack, T. K. and Thompson, A. M.: Remote Sensing of Tropospheric  
421 Pollution from Space, *Bull. Am. Meteorol. Soc.*, 89(6), 805–821,  
422 doi:10.1175/2008BAMS2526.1, 2008.

423 de Foy, B., Lu, Z., Streets, D. G., Lamsal, L. N. and Duncan, B. N.: Estimates of power plant NO  
424 x emissions and lifetimes from OMI NO<sub>2</sub> satellite retrievals, *Atmos. Environ.*, 116, 1–11, 2015.

425 Geddes, J. A. and Martin, R. V.: Global deposition of total reactive nitrogen oxides from 1996 to  
426 2014 constrained with satellite observations of NO<sub>2</sub> columns, *Atmos. Chem. Phys.*, 17(16),



427 10071–10091, doi:10.5194/acp-17-10071-2017, 2017.

428 Ghude, S. D., Pfister, G. G., Jena, C., van der A, R. J., Emmons, L. K. and Kumar, R.: Satellite  
429 constraints of nitrogen oxide (NO<sub>x</sub>) emissions from India based on OMI observations and WRF-  
430 Chem simulations, *Geophys. Res. Lett.*, 40(2), 423–428, 2013.

431 Henze, D. K., Hakami, A. and Seinfeld, J. H.: Development of the adjoint of GEOS-Chem,  
432 *Atmos. Chem. Phys.*, 7(9), 2413–2433, doi:10.5194/acp-7-2413-2007, 2007.

433 Henze, D. K., Seinfeld, J. H. and Shindell, D. T.: Inverse modeling and mapping US air quality  
434 influences of inorganic PM 2.5 precursor emissions using the adjoint of GEOS-Chem, *Atmos.*  
435 *Chem. Phys.*, 9(16), 5877–5903, 2009.

436 Ingmann, P., Veihelmann, B., Langen, J., Lamarre, D., Stark, H. and Courrèges-Lacoste, G. B.:  
437 Requirements for the GMES Atmosphere Service and ESA’s implementation concept: Sentinels-  
438 4/-5 and -5p, *Remote Sens. Environ.*, 120, 58–69, doi:10.1016/j.rse.2012.01.023, 2012.

439 Kharol, S. K., Shephard, M. W., McLinden, C. A., Zhang, L., Sioris, C. E., O’Brien, J. M., Vet,  
440 R., Cady-Pereira, K. E., Hare, E., Siemons, J. and Krotkov, N. A.: Dry Deposition of Reactive  
441 Nitrogen From Satellite Observations of Ammonia and Nitrogen Dioxide Over North America,  
442 *Geophys. Res. Lett.*, 45(2), 1157–1166, doi:10.1002/2017GL075832, 2018.

443 Kim, J.: GEMS (Geostationary Environment Monitoring Spectrometer) onboard the  
444 GeoKOMPSAT to monitor air quality in high temporal and spatial resolution over Asia-Pacific  
445 Region, in EGU General Assembly Conference Abstracts, vol. 14, p. 4051., 2012.

446 Kuhns, H., Knipping, E. M. and Vukovich, J. M.: Development of a United States–Mexico  
447 emissions inventory for the big bend regional aerosol and visibility observational (BRAVO)  
448 study, *J. Air Waste Manage. Assoc.*, 55(5), 677–692, 2005.

449 Lamsal, L. N., Martin, R. V., Van Donkelaar, A., Celarier, E. A., Bucsela, E. J., Boersma, K. F.,  
450 Dirksen, R., Luo, C. and Wang, Y.: Indirect validation of tropospheric nitrogen dioxide retrieved  
451 from the OMI satellite instrument: Insight into the seasonal variation of nitrogen oxides at  
452 northern midlatitudes, *J. Geophys. Res. Atmos.*, doi:10.1029/2009JD013351, 2010.

453 Lamsal, L. N., Martin, R. V., Padmanabhan, A., van Donkelaar, A., Zhang, Q., Sioris, C. E.,  
454 Chance, K., Kurosu, T. P. and Newchurch, M. J.: Application of satellite observations for timely  
455 updates to global anthropogenic NO<sub>x</sub> emission inventories, *Geophys. Res. Lett.*, 38(5), 2011.

456 Laughner, J. L. and Cohen, R. C.: Direct observation of changing NO<sub>x</sub> lifetime in North  
457 American cities, *Science (80-. )*, 366(6466), 723–727, doi:10.1126/science.aax6832, 2019.

458 Laughner, J. L., Zare, A. and Cohen, R. C.: Effects of daily meteorology on the interpretation of  
459 space-based remote sensing of NO<sub>2</sub>, *Atmos. Chem. Phys.*, 16, 15247–15264, doi:10.5194/acp-  
460 16-15247-2016, 2016.

461 Lorente, A., Folkert Boersma, K., Yu, H., Dörner, S., Hilboll, A., Richter, A., Liu, M., Lamsal,  
462 L. N., Barkley, M., De Smedt, I., Van Roozendaal, M., Wang, Y., Wagner, T., Beirle, S., Lin, J.-  
463 T., Krotkov, N., Stammes, P., Wang, P., Eskes, H. J. and Krol, M.: Structural uncertainty in air  
464 mass factor calculation for NO<sub>2</sub> and HCHO satellite retrievals, *Atmos. Meas. Tech.*, 10(3), 759–  
465 782, doi:10.5194/amt-10-759-2017, 2017.

466 Martin, R. V., Jacob, D. J., Chance, K., Kurosu, T. P., Palmer, P. I. and Evans, M. J.: Global  
467 inventory of nitrogen oxide emissions constrained by space-based observations of NO<sub>2</sub> columns,  
468 *J. Geophys. Res.*, 108(D17), 4537, doi:10.1029/2003JD003453, 2003.

469 Martin, R. V., Chance, K., Jacob, D. J., Kurosu, T. P., Spurr, R. J. D., Bucsela, E., Gleason, J. F.,  
470 Palmer, P. I., Bey, I. and Fiore, A. M.: An improved retrieval of tropospheric nitrogen dioxide  
471 from GOME, *J. Geophys. Res. Atmos.*, 107(D20), 4437, doi:10.1029/2001JD001027, 2002a.

472 Martin, R. V., Jacob, D. J., Logan, J. A., Bey, I., Yantosca, R. M., Staudt, A. C., Li, Q., Fiore, A.  
473 M., Duncan, B. N. and Liu, H.: Interpretation of TOMS observations of tropical tropospheric  
474 ozone with a global model and in situ observations, *J. Geophys. Res. Atmos.*, 107(D18), 2002b.

475 Murray, L. T., Jacob, D. J., Logan, J. A., Hudman, R. C. and Koshak, W. J.: Optimized regional  
476 and interannual variability of lightning in a global chemical transport model constrained by  
477 LIS/OTD satellite data, *J. Geophys. Res. Atmos.*, 117(D20), 2012.

478 Olivier, J. G. J., Van Aardenne, J. A., Dentener, F. J., Pagliari, V., Ganzeveld, L. N. and Peters,  
479 J. A. H. W.: Recent trends in global greenhouse gas emissions: regional trends 1970–2000 and  
480 spatial distribution of key sources in 2000, *Environ. Sci.*, 2(2–3), 81–99, 2005.

481 Palmer, P. I., Jacob, D. J., Chance, K. and Martin, R. V.: Air mass factor formulation for  
482 spectroscopic measurements from satellites’ Application to formaldehyde retrievals from the  
483 Global Ozone Monitoring Experiment, *J. Geophys. Res.*, 106(D13), 14,539-14550,  
484 doi:10.1029/2000JD900772, 2001.

485 Park, R. J., Jacob, D. J., Field, B. D., Yantosca, R. M. and Chin, M.: Natural and transboundary  
486 pollution influences on sulfate-nitrate-ammonium aerosols in the United States: Implications for  
487 policy, *J. Geophys. Res. Atmos.*, 109(D15), 2004.

488 Qu, Z., Henze, D. K., Capps, S. L., Wang, Y., Xu, X., Wang, J. and Keller, M.: Monthly top-

489 down NO<sub>x</sub> emissions for China (2005-2012): A hybrid inversion method and trend analysis, J.  
490 Geophys. Res. Atmos., doi:10.1002/2016JD025852, 2017.

491 Qu, Z., Henze, D. K., Theys, N., Wang, J. and Wang, W.: Hybrid mass balance/4D-Var joint  
492 inversion of NO<sub>x</sub> and SO<sub>2</sub> emissions in East Asia, J. Geophys. Res. Atmos., 2018JD030240,  
493 doi:10.1029/2018JD030240, 2019.

494 Rodgers, C. D. and Connor, B. J.: Intercomparison of remote sounding instruments, J. Geophys.  
495 Res. Atmos., 108(D3), 2003.

496 Spurr, R. J. D.: Simultaneous derivation of intensities and weighting functions in a general  
497 pseudo-spherical discrete ordinate radiative transfer treatment, J. Quant. Spectrosc. Radiat.  
498 Transf., 75(2), 129–175, doi:10.1016/S0022-4073(01)00245-X, 2002.

499 Streets, D. G., Zhang, Q., Wang, L., He, K., Hao, J., Wu, Y., Tang, Y. and Carmichael, G. R.:  
500 Revisiting China's CO emissions after the transport and chemical evolution over the Pacific  
501 (TRACE-P) mission: synthesis of inventories, atmospheric modeling, and observations, J.  
502 Geophys. Res. Atmos., 111(D14), 2006.

503 Streets, D. G., Canty, T., Carmichael, G. R., De Foy, B., Dickerson, R. R., Duncan, B. N.,  
504 Edwards, D. P., Haynes, J. A., Henze, D. K., Houyoux, M. R., Jacob, D. J., Krotkov, N. A.,  
505 Lamsal, L. N., Liu, Y., Lu, Z., Martin, R. V., Pfister, G. G., Pinder, R. W., Salawitch, R. J. and  
506 Wecht, K. J.: Emissions estimation from satellite retrievals: A review of current capability,  
507 Atmos. Environ., 77, 1011–1042, doi:10.1016/j.atmosenv.2013.05.051, 2013.

508 Vinken, G. C. M., Boersma, K. F., Maasakkers, J. D., Adon, M. and Martin, R. V.: Worldwide  
509 biogenic soil NO<sub>x</sub> emissions inferred from OMI NO<sub>2</sub> observations, Atmos. Chem. Phys.,  
510 doi:10.5194/acp-14-10363-2014, 2014.

511 Wang, Y., Jacob, D. J. and Logan, J. A.: Global simulation of tropospheric O<sub>3</sub>-NO<sub>x</sub>-  
512 hydrocarbon chemistry: 1. Model formulation, J. Geophys. Res. Atmos., 103(D9), 10713–10725,  
513 1998.

514 Van der Werf, G. R., Randerson, J. T., Giglio, L., Collatz, G. J., Mu, M., Kasibhatla, P. S.,  
515 Morton, D. C., DeFries, R. S., Jin, Y. van and van Leeuwen, T. T.: Global fire emissions and the  
516 contribution of deforestation, savanna, forest, agricultural, and peat fires (1997–2009), Atmos.  
517 Chem. Phys., 10(23), 11707–11735, 2010.

518 Xu, X., Wang, J., Henze, D. K., Qu, W. and Kopacz, M.: Constraints on aerosol sources using  
519 GEOS-Chem adjoint and MODIS radiances, and evaluation with multisensor (OMI, MISR) data,

520 J. Geophys. Res. Atmos., 118(12), 6396–6413, doi:10.1002/jgrd.50515, 2013.

521 Zhang, L., Shao, J., Lu, X., Zhao, Y., Hu, Y., Henze, D. K., Liao, H., Gong, S. and Zhang, Q.:  
522 Sources and Processes Affecting Fine Particulate Matter Pollution over North China: An Adjoint  
523 Analysis of the Beijing APEC Period, Environ. Sci. Technol., 50(16), 8731–8740,  
524 doi:10.1021/acs.est.6b03010, 2016.

525 Zhu, L., Jacob, D. J., Kim, P. S., Fisher, J. A., Yu, K., Travis, K. R., Mickley, L. J., Yantosca, R.  
526 M., Sulprizio, M. P., De Smedt, I., González Abad, G., Chance, K., Li, C., Ferrare, R., Fried, A.,  
527 Hair, J. W., Hanisco, T. F., Richter, D., Jo Scarino, A., Walega, J., Weibring, P. and Wolfe, G.  
528 M.: Observing atmospheric formaldehyde (HCHO) from space: validation and intercomparison  
529 of six retrievals from four satellites (OMI, GOME2A, GOME2B, OMPS) with SEAC4RS  
530 aircraft observations over the southeast US, Atmos. Chem. Phys., 16(21), 13477–13490,  
531 doi:10.5194/acp-16-13477-2016, 2016.

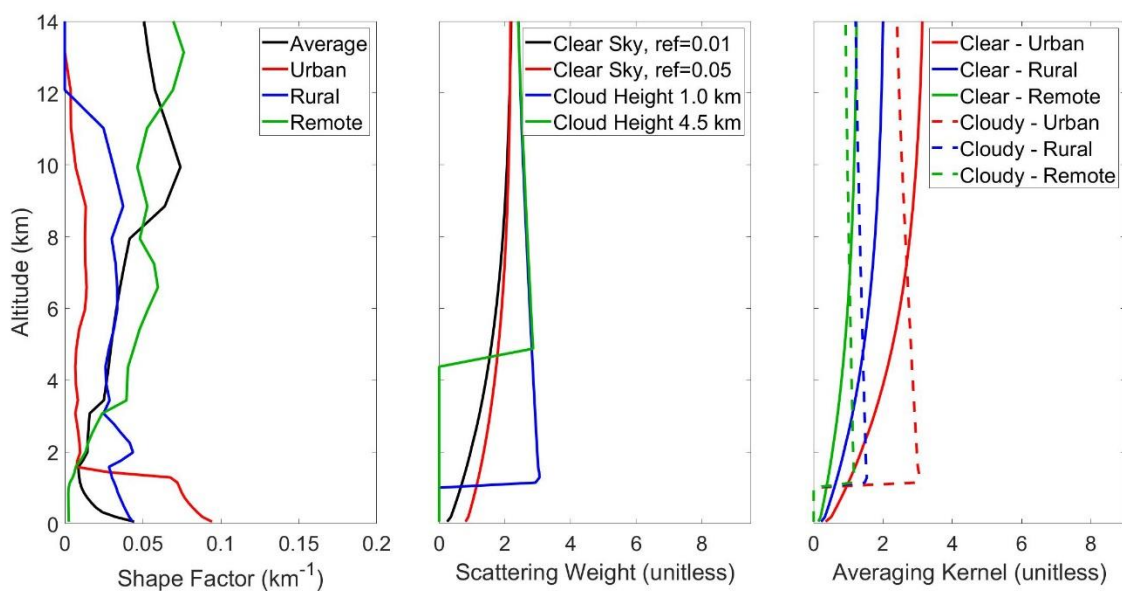
532 Zoogman, P., Liu, X., Suleiman, R. M., Pennington, W. F., Flittner, D. E., Al-Saadi, J. A.,  
533 Hilton, B. B., Nicks, D. K., Newchurch, M. J., Carr, J. L., Janz, S. J., Andraschko, M. R., Arola,  
534 A., Baker, B. D., Canova, B. P., Chan Miller, C., Cohen, R. C., Davis, J. E., Dussault, M. E.,  
535 Edwards, D. P., Fishman, J., Ghulam, A., González Abad, G., Grutter, M., Herman, J. R., Houck,  
536 J., Jacob, D. J., Joiner, J., Kerridge, B. J., Kim, J., Krotkov, N. A., Lamsal, L., Li, C., Lindfors,  
537 A., Martin, R. V., McElroy, C. T., McLinden, C., Natraj, V., Neil, D. O., Nowlan, C. R.,  
538 O’Sullivan, E. J., Palmer, P. I., Pierce, R. B., Pippin, M. R., Saiz-Lopez, A., Spurr, R. J. D.,  
539 Szykman, J. J., Torres, O., Veefkind, J. P., Veihelmann, B., Wang, H., Wang, J. and Chance, K.:  
540 Tropospheric emissions: Monitoring of pollution (TEMPO), J. Quant. Spectrosc. Radiat. Transf.,  
541 186, 17–39, doi:10.1016/j.jqsrt.2016.05.008, 2017.

542

543

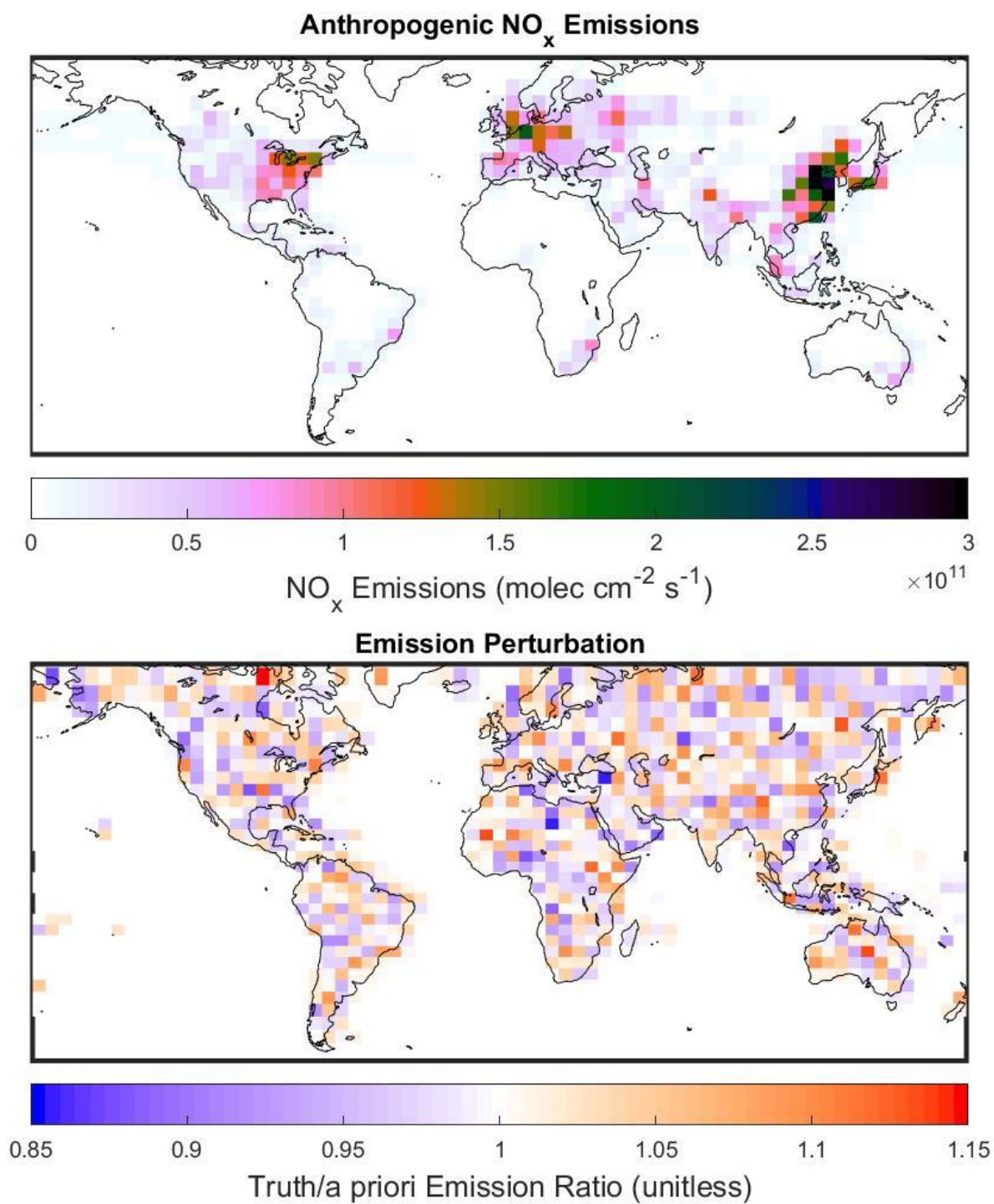
544 Figures:

545

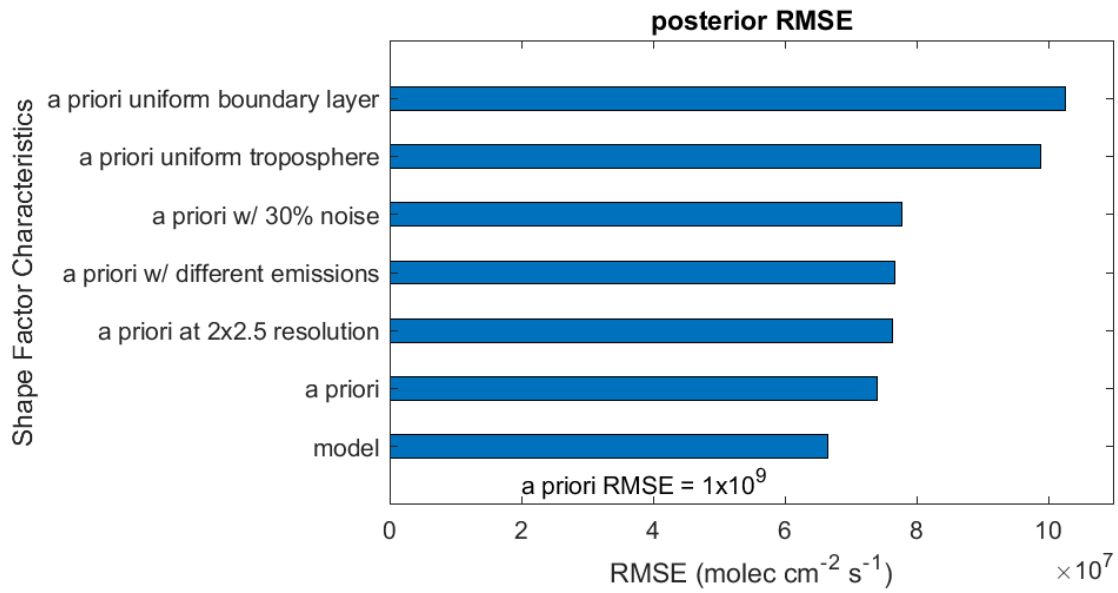


546

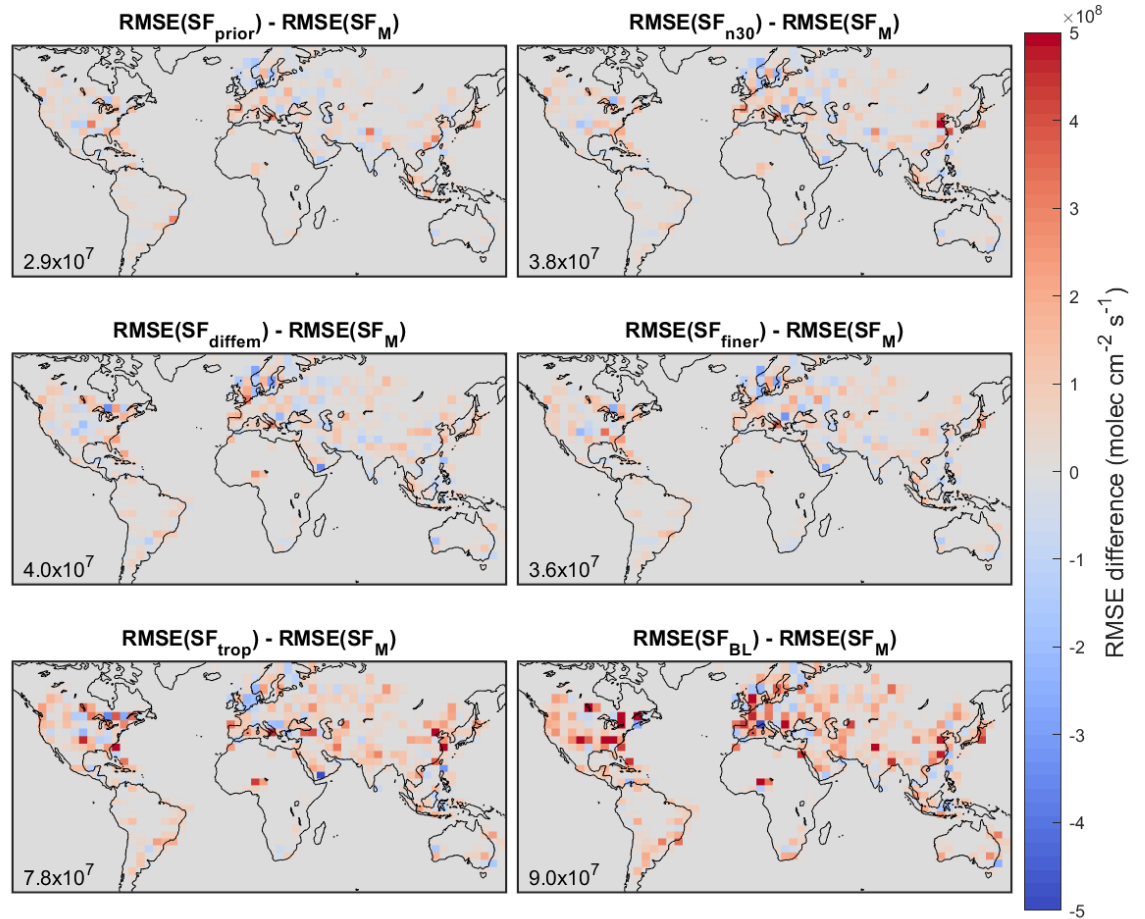
547 Figure 1: (Left) Shape factor profiles from a GEOS-Chem simulation for July 2010. Shown are a  
548 global average, and typical urban (Beijing), rural (Midwest USA), and remote (Tropical Pacific)  
549 profiles. (Middle) Typical OMI scattering weight profiles for varying surface reflectance and  
550 cloud height. (Right) Averaging kernels calculated using the same shape factors and scattering  
551 weights (“Clear Sky” surface reflectance is 0.01, “Cloudy” uses cloud height of 1 km).



553  
554 Figure 2 (top) Anthropogenic NO<sub>x</sub> emissions for July 2010 used in GEOS-Chem. (bottom) Ratio  
555 of "true" emissions used to create *Obs<sub>S</sub>* synthetic observations to a priori NO<sub>x</sub> emissions.  
556

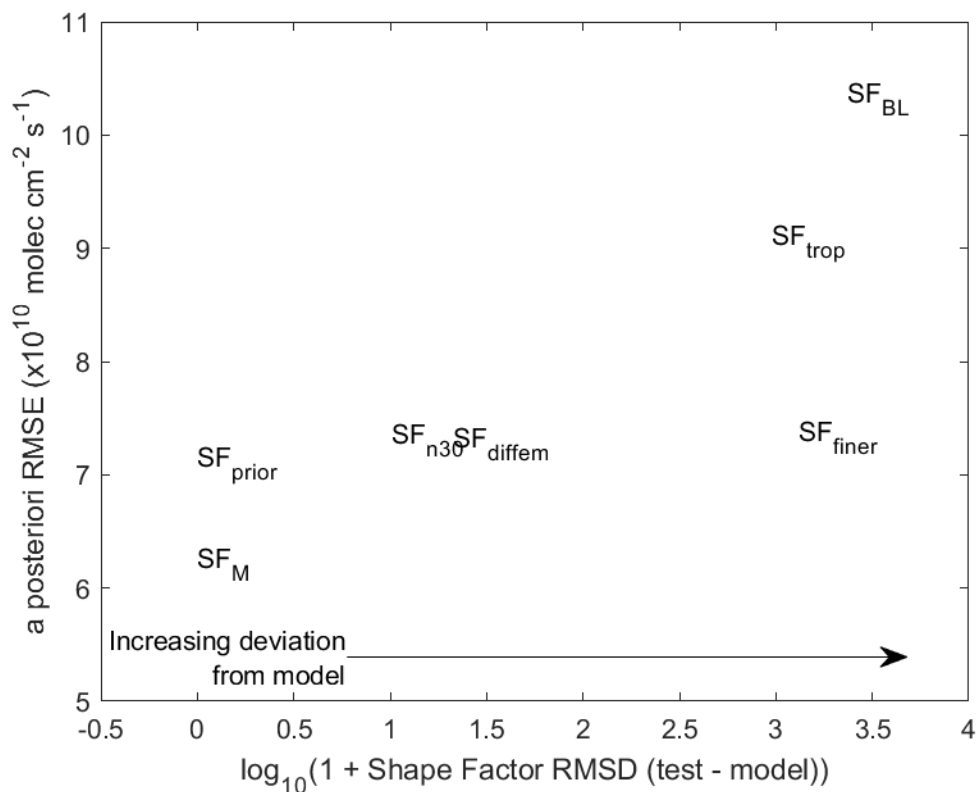


557  
 558 Figure 3: Global root mean square error (RMSE) values for 4D-Var estimates of  $\text{NO}_x$  emissions  
 559 for tests using various shape factors in AMF calculations.  
 560



561  
 562 Figure 4: Difference between root mean square error (RMSE) of adjoint tests for  $Obs_5$  synthetic  
 563 observations. Root mean square differences between the *a posteriori* emissions estimates  
 564 ( $\text{molec}/\text{cm}^2/\text{s}$ ) are inset.  
 565





566  
 567 Figure 5: Scatterplot of adjoint test results. X-axis represents the deviation of the shape factor  
 568 from the model simulated shape factor (root mean square difference). Y-axis represents the *a*  
 569 *posteriori* emissions error from the adjoint inversion.

570

571

Variable	<i>Palmer et al., 2001</i>	<i>Eskes &amp; Boersma, 2003</i>	<i>Boersma et al., 2016</i>	Notation used here
Air mass factor	AMF	M	M	M
Slant Column	$\Omega_S$	S	$N_S$	$\Omega_s$
Vertical Column	$\Omega_V$	V	$N_V$	$\Omega_v$
Scattering Weight	w(z)	$C_1$	$m_1$	W
Shape Factor	$S_z(z)$			S(z)
Averaging Kernel		A	A	A
Number density	n(z)	X	$x_1$	n(z)
Geometric AMF	AMF <sub>G</sub>			M <sub>G</sub>

572 Table 1: Lexicon comparing notation used in this paper to that used in previous studies.

573

574

575

576

Test name	Shape factor source	Air Mass Factor (unitless) Global Mean	Synthetic observation ( <i>Obs<sub>S</sub></i> ) vertical column density ( $\times 10^{15}$ molec/cm <sup>2</sup> )	
			Global Mean ( $\times 10^{15}$ molec/cm <sup>2</sup> )	Maximum difference from SF <sub>M</sub> (%)
SF <sub>M</sub>	Model	2.1	0.9	-
SF <sub>n30</sub>	Model w/ 30% noise	2.1	0.9	19
SF <sub>diffem</sub>	Model w/ different emissions	2.1	0.9	28
SF <sub>finer</sub>	Model at finer (2°x2.5°) resolution	1.6	1.2	23
SF <sub>trop</sub>	Uniform in troposphere	1.8	1.0	57
SF <sub>BL</sub>	Uniform in boundary layer	1.3	1.5	27

577 Table 2: Global mean air mass factors and synthetic observation vertical column density for  
578 shape factors tested here.

Test Name	Shape Factor Source	Correlation (r) of <i>a posteriori</i> error and “true” emissions	<i>a posteriori</i> RMSE ( $\times 10^8$ molec/cm <sup>2</sup> /s)		Error standard deviation ( $\times 10^8$ molec/cm <sup>2</sup> /s)		Maximum error ( $\times 10^9$ molec/cm <sup>2</sup> /s)
		if “true” emissions $> 10^{10}$ molec/cm <sup>2</sup> /s	“true” emissions $> 10^{10}$ molec/cm <sup>2</sup> /s	“true” emissions $> 10^{11}$ molec/cm <sup>2</sup> /s	“true” emissions $> 10^{10}$ molec/cm <sup>2</sup> /s	“true” emissions $> 10^{11}$ molec/cm <sup>2</sup> /s	
SF <sub>M</sub>	Model	0.06*	1.8	3.0	1.8	2.9	1.6
SF <sub>prior</sub>	a priori	0.11	2.0	3.2	2.0	3.3	1.6
SF <sub>n30</sub>	Model w/ 30% noise	0.26	2.1	3.9	2.1	3.8	1.8
SF <sub>diffem</sub>	Model w/ different emissions	0.13	2.0	3.6	2.0	3.7	1.9
SF <sub>finer</sub>	Model at finer (2°x2.5°) resolution	0.05*	2.1	3.2	2.1	3.2	1.8
SF <sub>trop</sub>	Uniform in troposphere	0.39	2.8	5.6	2.8	5.5	2.1
SF <sub>BL</sub>	Uniform in boundary layer	0.17	2.8	4.6	2.8	4.6	1.9

580 Table 3: Summary of error statistics for adjoint tests. Values marked \* indicate that correlation is  
581 not statistically significant ( $p > 0.05$ ). For comparisons, mean “true” emissions for grid boxes with  
582 emissions  $> 10^{10}$  molec/cm<sup>2</sup>/s is  $4.9 \times 10^{10}$ , and mean “true” emissions for boxes with  
583 emissions  $> 10^{11}$  molec/cm<sup>2</sup>/s is  $1.6 \times 10^{11}$  molec/cm<sup>2</sup>/s.